

Image Reconstruction from Highly Sparse and Limited Angular Diffraction Tomography Using Compressed Sensing Approach

Pavel Roy Paladhi^{1, *}, Amin Tayebi^{1, 2}, Portia Banerjee¹, Lalita Udpa¹, and Satish Udpa¹

Abstract—Diffraction tomography (DT) from limited projection data has been an active research topic for over three decades. The interest has been steadily fueled due to its application in multiple disciplines including medical imaging, structural health monitoring and non-destructive evaluation to name a few. This paper explores the applicability of compressed sensing to recover complex-valued objective functions (e.g., complex permittivity in microwave tomography). Generally, compressed sensing based tomographic reconstruction has been studied under full angular access. In this paper, the effect of lowering the angular access in addition to highly limited number of projection data is explored. The effectiveness of the reconstruction methods is tested with severely limited dataset which would render reconstruction impossible by traditional iterative approximation methods. Furthermore, results show that complex-valued phantoms can be reconstructed from as few as 15 projections from 120° coverage, a significant finding. In this study, the Total Variation (TV) has been used as the l_1 norm within the compressed sensing framework. The robustness of the algorithm in presence of noise is discussed. Use of multiple sparse domains has also been explored briefly. The results show the effectiveness of TV as a regularization parameter even for complex-valued images under the compressed sensing regime. This is a pertinent observation as TV is a simple norm to implement. For a large class of images, especially in medical imaging, this implies the availability of a steady l_1 norm for easy implementation of compressed sensing reconstruction for complex-valued images.

1. INTRODUCTION

Diffraction Tomography is a popular imaging technique with highly multidisciplinary applications. It is a broad imaging modality of which ultrasound and microwave tomographic imaging are sub-classes. Unlike Computed Tomography (CT) which assumes straight line propagation of the incident waves, DT incorporates the diffracting nature of the interrogating energy and can be used to recover complex-valued objective functions or images. In the presence of weak scatterers, assuming the Born or Rytov approximations [1], the Fourier Diffraction Projection theorem (FDP) relates the scattered field data from the Region of Interest (ROI) to the 2D-Fourier Space of the ROI. This scattered field data or the projection data from multiple angles can be used to populate the Fourier space of the object (ROI). The ROI is reconstructed from this Fourier data through Fourier inversion or backpropagation techniques. A major obstacle in many real life scenarios is that projection measurements cannot be gathered over full 360° view around the test object. Reconstruction from this partial data leads to many artifacts and loss of important features in the resulting image. Thus, specialized schemes are needed for image reconstruction from limited angular coverage projection data. If the angular coverage is moderately limited, between 180°–270°, the authors had recently proposed generalized algorithms which exploit redundancy in the projection data [2–5]. This is a direct backpropagation based method

Received 15 November 2016, Accepted 11 January 2017, Scheduled 25 January 2017

* Corresponding author: Pavel Roy Paladhi (roypalad@egr.msu.edu).

¹ Department of Electrical and Computer Engineering, Michigan State University, 428 S Shaw Lane, Rm-2120, East Lansing, Michigan 48824, USA. ² Department of Physics and Astronomy, Michigan State University, East Lansing, Michigan 48824, USA.

which can handle moderate limitations in coverage. However, for highly sparse data or limited angular access various minimization, regularization, estimation techniques and statistical approaches have to be utilized and indeed, these approaches are being successfully explored to make the reconstruction algorithms more robust to sparse and noisy data, e.g., [6, 7]. A recent and highly popular development in the domain of sparse recovery is the field of compressed sensing (CS) [8–11]. The allure of this field arises from the fact that under certain constraints (i.e., if the data acquisition and signal recovery procedure conforms to the CS formulation), it can ensure that exact recovery is possible in highly under-determined systems. Thus a few projections are sufficient to create an almost distortion free reconstruction. Hence it is of great importance in all applications dealing with highly limited projection data as in medical imaging [12–17], data channel sampling [18], radar imaging [19–21], spectrum sensing in cognitive radio systems [22] and many other applications. A steady focus is also directed towards improving the data acquisition and reconstruction frameworks for increasing the present capabilities of compressed sensing [23–25].

This paper explores CS based reconstruction for complex-valued objective functions under the domain of diffraction tomography. It is organized as follows: Section 2 briefly introduces DT basics and the field of compressed sensing, Section 3 sets up Sparse Diffraction Tomography as a CS formulation, Section 4 sets up total variation as the l_1 penalty term for CS based DT reconstruction and provides detailed results and analysis of performance of using TV as the penalty term in CS, Section 5 briefly explores the feasibility of using multiple sparse domains in CS based reconstruction and finally Section 6 concludes the paper summarizing the findings and their impact.

2. BACKGROUND

2.1. Diffraction Tomography

The fundamental theory underlying 2D-DT is the FDP which relates the scattered field data from the ROI due to incident plane waves to the 2D-Fourier space of the ROI [1]. The traditional 2D-configuration is shown in Fig. 1 [4], where the object $f(x, y)$ is illuminated with a monochromatic plane wave of frequency ν_0 incident at an angle ϕ to the horizontal axis. The 1D Fourier Transform (FT) of the scattered field measured along the straight line $\eta = l$ in the co-ordinate system (ξ, η) gives the values of the 2D transform of the object $F(\nu_x, \nu_y)$ along a semi-circular arc in the frequency domain, at angle ϕ as shown in the right half of Fig. 1. The scattered field data and the object function are related by the following equation:

$$U(\nu, l) = \frac{j}{2\sqrt{\nu_0^2 - \nu^2}} e^{j\sqrt{\nu_0^2 - \nu^2}l} F\left(\nu, \sqrt{\nu_0^2 - \nu^2} - \nu_0\right), \quad (1)$$

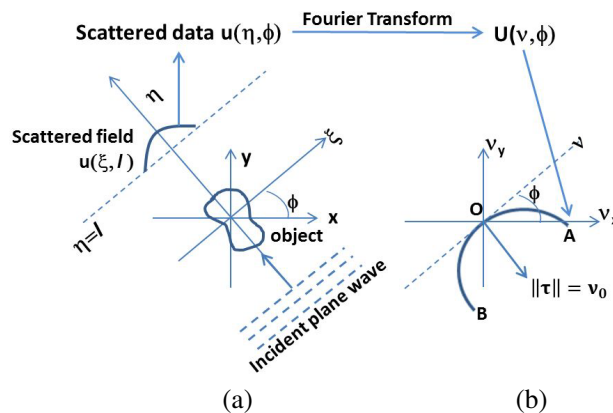


Figure 1. (a) Classical scan configuration of 2D DT and (b) relation of scattered field data with the 2D Fourier space of the objective function.

where $U(\nu, l)$ represents 1D FT of the scattered field, $u(\xi, \eta)$ under Born approximation (measured on line $\eta = l$), and ν lies in the range $[-\nu_0, \nu_0]$.

This relates the scattered field from a single projection to Fourier space data of the object function being investigated. Multiple projections, i.e., scattered field data from incident excitation from different angles can then be used to get Fourier domain information of the ROI. Traditional reconstruction techniques such as filtered backpropagation (FBPP) [26] and Fourier inversion use this projection data from $[0, 2\pi]$ angular coverage for accurate image recovery. Though the formulation applies to weak scatterers, it is widely used and since its introduction, a steady research focus has been maintained on this topic [27–33]. Present day research on DT focuses on image recovery from projection data obtained under constraints of angular coverage and/or the number of available projections. Many regularization and optimization techniques have been explored and developed to solve this under-determined system. However recently, with the advent of compressed sensing theory, a natural interest has developed in performing DT image recovery under the CS regime. This paper explores DT reconstruction algorithms under this CS regime for complex valued image recovery.

2.2. Compressed Sensing (CS)

The fundamental concept underlying compressed sensing (CS) is the successful exploitation of a sparse representation of the signal to be recovered. That is, even if the signal itself is not sparse, it might be expressed as a sparse signal in some other domain. The sparsity in this alternate domain can then be exploited in CS based algorithms.

Consider a sensing matrix Φ , representing the data acquisition system. For example, in tomography, Φ is the Fourier matrix. Let Φ directly compress the signal while *sensing* it. That is, a small number of measurements (e.g., projection data in tomography) retain all the information within the original signal. Also, let it be a linear measurement process that collects M datapoints ($M < N$) and N being the dimension of the signal to be recovered. Then Φ is a $M \times N$ matrix and the output y is an inner product of the signal x with the columns of Φ . Then if Ψ be a sparse basis of x , we can write

$$y = \Phi x = \Phi \Psi s = \Theta s \quad (2)$$

where $\Theta := \Phi \Psi$ is an $M \times N$ matrix. The measurement or *sensing* matrix Φ is fixed and independent of x . In traditional theory, since $M < N$, the system in Eq. (2) is under determined and in general the solution is ill-posed. However, the sparsity of x in the Ψ domain alleviates this issue.

CS aims to reduce the number of minimum measurements required to completely describe a signal by exploiting its *compressibility*. This can be expressed in terms of sparsity of a signal. A S -sparse signal $x \in \mathbb{C}^n$ is a signal which has at most S non-zero elements. The goal is to be able to completely reconstruct a S -sparse signal x of dimension n from M measurements where $M \approx S$ or marginally more. In order to do this, the measurement (or data acquisition), signal handling and image recovery (reconstruction) has to be formulated in the proper CS framework and adhering to specific constraints. These are actually the very conditions which enable us to defeat the Shannon sampling rate on a grand scale. These requirements are briefly enumerated below:

- The signal of interest x should be sparse or compressible in some domain.
- A stable measurement matrix Φ must be available which can transform the S -sparse signal $x \in \mathbb{C}^N$ to $y \in \mathbb{C}^M$ without any loss of information due to the dimensional reduction from N to M . This condition of Φ is often referred to as the Restricted Isometry Property (RIP) [34].
- A reconstruction algorithm which can recover the original signal from the measurements y . For compressed sensing framework, l_1 -norm minimization is the de-facto algorithm of choice.

As CS aims to exploit sparsity, the logical approach would be to solve an l_0 norm minimization problem, which is an N_p hard problem. However, most of the signal recovery related work in compressed sensing explores the use of l_1 as a substitute of l_0 norm. An l_1 minimization problem can be solved as a linear program and because of the greatly reduced computational complexity, is always preferable over an l_0 norm minimization. This is possible because fortunately, in [35], it was shown that for a K -sparse signal, if the measurement size M satisfies

$$M \geq cK \log(N/\delta) \quad (3)$$

where c is a constant, then with probability more than $1 - \delta$, the solution to the l_1 minimization problem:

$$\hat{s} = \operatorname{argmin} \|s'\|_1, \quad \text{such that } \Theta s' = y \quad (4)$$

is the desired original signal. In the presence of noise, the constraint is just $\|\Theta s'y\|_2 \leq \varepsilon$ with ε being a tolerance parameter. The l_1 minimization problem can be recast as a convex optimization problem as:

$$\hat{s} = \operatorname{argmin} \|y - \Theta s'\|_1 \quad (5)$$

This can be conveniently solved, e.g., as a linear program called *basis pursuit*, which has $O(N^3)$ computational complexity [8, 11]. A very well researched minimization problem is to minimize the following functional:

$$F_\tau(x) \equiv \|\Phi x - y\|_2^2 + 2\tau \|x\|_1 \quad (6)$$

with $\tau > 0$ and bounded above. This is an unconstrained convex optimization problem. It has been shown [36] that a solution to Eq. (4) would also minimize Eq. (6). Thus many well investigated convex optimization algorithms can be applied to solve an l_1 minimization problem.

A curious fact is that many physical signals of interest do in fact abide by these conditions. Hence, compressed sensing is applicable to a variety of scenarios. Thus, the development of this new theory gained a huge impetus over the last few years. It has become one of the most hotly researched topics under image reconstruction algorithms.

To show the effectiveness of CS over traditional methods, before delving further, reconstructions from a regular Least Squares approach (LS) and CS based reconstruction from 20 views (or projections) and 150° coverage have been compared in Fig. 2. A complex-valued phantom has been reconstructed. The real part of the original image is shown in Fig. 2(a), the imaginary part in Fig. 2(d). The real and imaginary parts have been purposefully made different to see the effect of reconstruction on both these components individually. This image is also the reference image for all the other reconstructions shown in this paper. This is the same phantom used by the authors as the reference image in [4]. As can be seen, the traditional LS method fails drastically under the severe limitations, whereas the CS based reconstruction reproduces the image with no major distortions and retaining all the major features of the image.

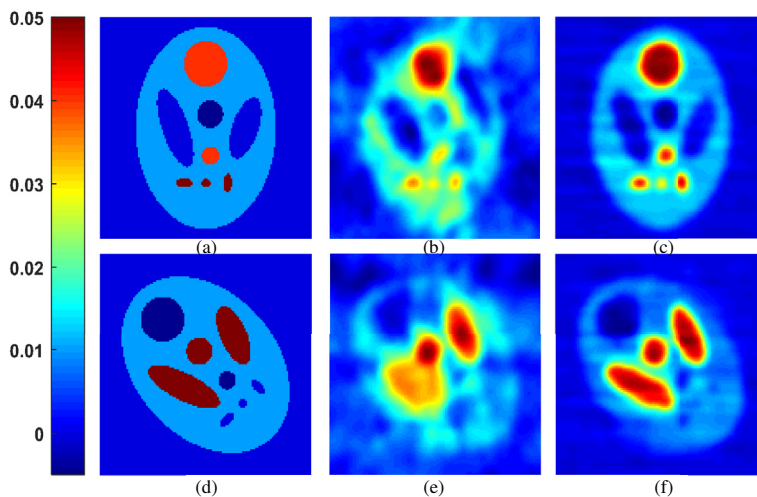


Figure 2. Effect of reconstruction from highly sparse data in traditional and compressed sensing based reconstructions of complex image from 20 views and 150° coverage: (a) real part of original image, (b) real part from LS recovery, (c) real part from CS recovery, (d) imaginary part of original image, (e) imaginary part from LS recovery, and (f) imaginary part from CS recovery.

3. CS BASED RECONSTRUCTION FOR DT

The projection data acquisition in diffraction tomography can be expressed as

$$F = \Phi(f) \quad (7)$$

where Φ is the diffraction operator, F the sampled data in k -space and f the object function. If the acquired data is highly sparse, then classical interpolation methods are no longer applicable as the Nyquist limit is not met. FBPP alone results in a lot of artifacts in the reconstructed image and distorts actual features in the image. However, under a compressed sensing framework, high quality reconstruction from sparse view data can still be achieved. Firstly, it is assumed that f , the signal to be recovered, is approximately sparse in some domain Ψ , such that $f = \Psi s$ as in previous section. Then, with the availability of F , knowledge of Φ and Ψ , we can formulate a convex optimization problem using the functional in Eq. (6):

$$\min_s \{ \|y - \Theta s\|_2^2 + \alpha \|s\|_1 \} \quad (8)$$

where α is the regularization parameter.

3.1. Application of CS to Sparse DT Recovery

For ultrasound or microwave based DT, the data acquisition matrix is the partial Fourier matrix. The sparse view data is generated by randomly choosing view angles. These samples give the vector y of (4) and (8). For setting up the CS framework, the sensing matrix $\Theta = \Phi\Psi$ must be constructed with Ψ being the sparse basis for the object. Let the object function be denoted by f , so that $f(x, y)$ can be used to represent the spatial distribution of the object function. The object has a bounded support, say $[-C, C] \times [-C, C]$, i.e., $f(x, y) = 0$ for $|x|, |y| > C$. Let f_d denote the discretized object function which is to be reconstructed. $f_d \in \mathbb{C}^{n_d \times n_d}$, with $n_d = 2[C/T]$ with T being the sample period. Also, let $F(u, v)$ and $F_d(u, v)$ be the Fourier transforms of $f(x, y)$ and $f_d(n_1, n_2)$ respectively. Also, the receiver array will have limited number of elements. Let the discrete field be $\hat{u}_{s,\theta} = u_{s,\theta}(n\tau)$, where τ is the spatial sampling interval of the system. Let $\hat{U}_{s,\theta}(\kappa)$ and $U_{s,\theta}(\kappa)$ be the respective Fourier transforms. In the limit $\tau \rightarrow 0$, both the signals become equal. A point to note here is that the Fourier transform of the scattered field is related to the Fourier space of the object along semicircular arcs as mentioned in Subsection 2.1. Here, κ gives the projection of a point on the semicircular arc to its tangent at the origin. Also, θ is the angle of incidence. Then, invoking the FDP, we can have $\hat{U}_{s,\theta}(\kappa) \approx U_{s,\theta}(\kappa) = F(u, v) \approx F_d(u, v)$. Let $\Omega_1 = \theta_1, \theta_2, \dots, \theta_{N_1}$ be the set of view or projection angles over which $\hat{u}_{s,\theta}(n\tau)$ is obtained and from that $\hat{U}_{s,\theta}(\kappa)$ is calculated for $\forall \kappa \in \Omega_2 = \kappa_1, \kappa_2, \dots, \kappa_{N_2}$. Then, f_d can be reconstructed from the projection dataset $\hat{U}_{s,\theta}(\kappa) \mid (\theta, \kappa) \in (\Omega_1, \Omega_2)$ as [16]:

$$\frac{(T\kappa_0)^2 U_0}{2j\gamma} e^{j\gamma t} \sum_{n_1=-[C/T]}^{[C/T]} \sum_{n_2=-[C/T]}^{[C/T]} f_{d_{n_1, n_2}} e^{-2\pi j(n_1 u + n_2 v)T} = \hat{U}_{s,\theta}(\kappa) + n_{s,\theta}(\kappa) \quad (9)$$

This is expressible in a compact matrix equation form as $\Phi f_d = F + n$, where $\Omega = (\Omega_1, \Omega_2)$, $\Phi \in \mathbb{C}^{|\Omega| \times (n_d)^2}$, $f_d \in \mathbb{C}^{(n_d)^2}$, $(n_1, n_2) \leq |n_d/2|$, $F \in \mathbb{C}^{|\Omega|}$. From (9), the Φ for the minimization problem is obtained. Essentially, the summation expression in Eq. (9) gives the coefficients of a Fourier matrix. By FDPT, the spatial frequency samples are gathered along the arc AOB (see Fig. 1). As the angle of incidence varies, the arc revolves around in the Fourier space and describes a centered disk of radius $\sqrt{2}k_0$. So the reconstruction of the object is always a low-pass filtered version of the original image. The following steps would be used to assure that the CS framework is maintained:

- **Incoherence** will be maintained by using a random set of angles for the projection data. A partial Fourier matrix will be used, which ensures RIP of the sensing matrix.
- **Sparsity** will be exploited initially through image gradients in Section 4. Later, in Section 5 simultaneous exploitation of multiple sparse domains will also be explored briefly.

Let the sparse basis matrix be Ψ . Combining l_1 norm and data constraints in the minimization problem, the initial problem is of the form:

$$\min_s \{ G(s) = \|F - \Phi\Psi s\|_2^2 + \alpha \|s\|_1 \} \quad (10)$$

Here, F gives the spatial frequency samples, and s is the coefficients of f_d in the sparse basis Ψ . In the next section, the reconstruction algorithm from projection dataset is presented.

3.2. Reconstruction

A minimization problem involves reducing a cost function in a series of iterative steps starting from an initial value of the cost function. The key feature is how the cost function is updated at each iteration. A significant amount of literature on methods are available to minimize a cost function. In this paper, as the minimization problem is essentially a convex optimization problem, optimization toolkit from Boyd and Vanderbeghe [36] has been used.

The overall reconstruction algorithm sequentially follows these steps:

- Generate projection data from random view angles.
- Fourier space data along semi-circular trajectories is found applying the FDPT.
- Iterative reconstruction through l_1 minimization in the sparse domain is applied while preserving the data constraints.

In the next section, reconstructions have been performed using TV as the l_1 sparsity term. The performance of the reconstruction under varying degrees of limited data and angular access have been evaluated.

4. RECONSTRUCTION WITH TOTAL VARIATION AS L_1 PENALTY TERM

Most physical samples investigated tomographically, do in fact possess piecewise continuous property distribution. Particularly, biological specimens would fall under this category, where regions over extended areas would have no variations but rapidly vary in certain confined areas, such as edges of organs or boundaries between different tissue. These images themselves are not sparse, however, their gradient images are sparse.

This is one form of sparsity that can be exploited in a CS framework. The gradient magnitude image (GMI) is defined in terms of derivatives in the vertical and horizontal direction of the image. Let D_{n_1, n_2}^h and D_{n_1, n_2}^v denote the finite difference operators in the horizontal (h) and vertical (v) directions respectively. The gradient of the image is $\nabla f_d = [D_{n_1, n_2}^h, D_{n_1, n_2}^v] f_d = D f_d$, where $D = [D^v, D^h] = \Psi$ is the sparsity promoting operator. The gradient magnitude then becomes $|\nabla f_d| = \sqrt{(D_{n_1, n_2}^h f_d)^2 + (D_{n_1, n_2}^v f_d)^2}$.

The l_1 -norm of the gradient image has often been termed as the total variation (TV) of the image, which then can be defined as

$$TV(f_d) = \sum_{n_1, n_2} \sqrt{(D_{n_1, n_2}^h f_d)^2 + (D_{n_1, n_2}^v f_d)^2} \quad (11)$$

TV can be employed as a means to exploit sparsity of piecewise smooth objects. It has been already used as a regularizing term before, e.g., [6]. TV can be effective in suppressing Gibbs effect while preserving edges [37]. To use TV as the l_1 norm, in the minimization problem of Eq. (10), the sparse signal s is the GMI, so that $s = D(f_d)$ where D is the sparsity operator and by definition, $\|D(f_d)\|_1 = TV(f_d)$. In this case, Eq. (10) becomes

$$\min_s \{G(s) = \|F - \Theta s\|_2^2 + \alpha \|s\|_1 = \|F - \Phi D^* s\|_2^2 + \alpha TV(f_d)\} \quad (12)$$

with α being the regularization parameter for the TV term and $\Theta = \Phi D^*$. To avoid a zero denominator in the TV term, an approximation which is often employed is: $\|D_{n_1, n_2} f_d\| \approx \sqrt{(D_{n_1, n_2}^h f_d)^2 + (D_{n_1, n_2}^v f_d)^2} + \mu$, where μ is a small positive number. The second term in Eq. (12) is the data constraint term added to keep the problem as an unconstrained optimization problem. The parameter α determines the relative weightage of the data constraint term and the l_1 penalty term. The value of α needs to be carefully chosen. In most cases this value would be application specific. A standard approach is to plot a response of the two terms in the minimization term with respect to the variation of α . A sweep of α over a large range would generally give insight towards an optimal value. Over the range of the sweep generally as α increases, the l_1 -norm decreases whereas the error norm increases. A value of α is so chosen as to make the l_1 norm low enough without increasing

the error norm. For the reconstructions performed here, the value of α has been fixed at 0.2. Once the reconstruction problem is set up in the CS framework as shown here, the l_1 minimization is an optimization problem in standard form. It is efficient to use an optimization toolkit if applicable. For solving convex optimization problems expressed in standard forms, a host of optimization toolsets are already available. In this work, the minimization problem of Eq. (12) is solved using a convex optimization toolkit *cvx* by Boyd & Vanderberghe [36, 38]. A particular advantage of using this toolkit is that it can be used to solve the primal-dual problem with the Matlab based *SeDumi* toolkit [39]. The solution comes with a certificate of convergence in the form of the distance from the dual maximum and the duality gap. So the distance of the solution (i.e., minimum of the objective function achieved) from the theoretical lower limit is known.

4.1. Reconstruction with TV as l_1 Minimizer

As part of this research, reconstruction was performed on a complex-valued phantom structure shown in Figs. 2(a) and (d). The acquisition data F is computed by determining semi-circular trajectories in Fourier space based on the angle of the incident beam as prescribed in [6]. To incorporate effects of measurement noise, this projection data is injected with random noise with energy levels at 5% of the average energy in the projection data. This noise injected data is assumed to be a reasonable approximation of experimental data.

To see the effectiveness of TV as the l_1 penalty term, two types of data variation is analyzed. The first being the number of projections when the angular access is fixed. The second being the variation of total coverage for a fixed number of projections. In this exercise, the projection datasets are fixed at 15, 20, 30 and 45 views. The angular coverage limits are fixed at 180° , 150° , 120° and 90° . In the figures below, reconstructions of real and imaginary part of the phantom are shown separately for these aforementioned variations. The effect of both type of variations on the reconstruction error are presented separately.

In Fig. 3 and Fig. 4, reconstructions from 45 projections are presented. It is seen that for the first three coverages, the quality of the images is almost constant. At 90° coverage, the reconstruction

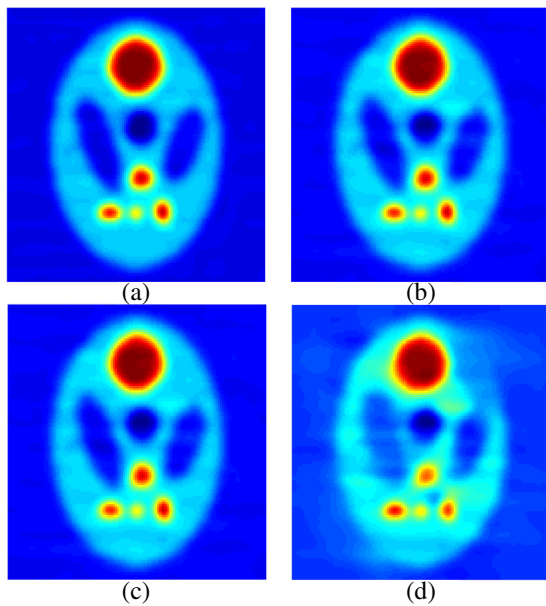


Figure 3. Reconstructions of real part of image with 45 views for different angular coverages: (a) 180° , (b) 150° , (c) 120° , and (d) 90° .

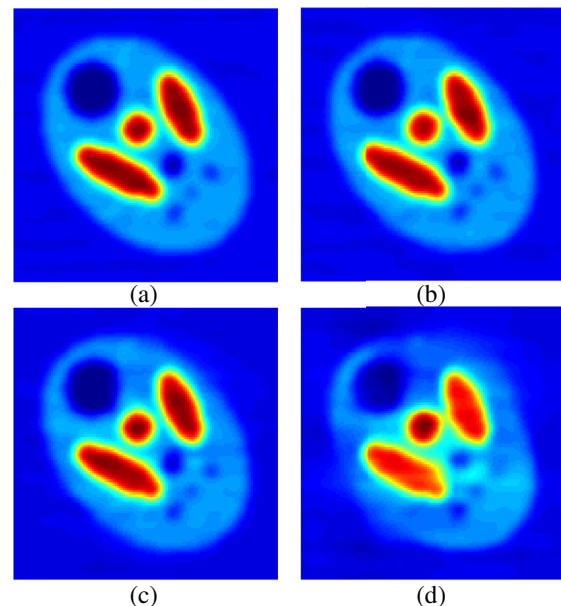


Figure 4. Reconstructions of imaginary part of image with 45 views for different angular coverages: (a) 180° , (b) 150° , (c) 120° , and (d) 90° .

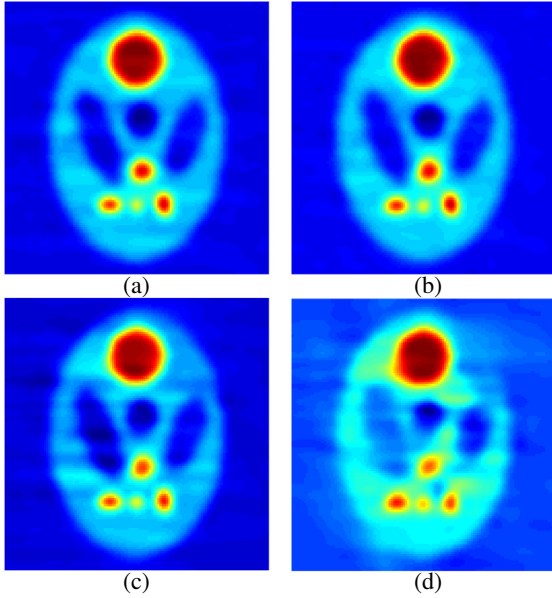


Figure 5. Reconstructions of real part of image with 30 views for different angular coverages: (a) 180°, (b) 150°, (c) 120°, and (d) 90°.

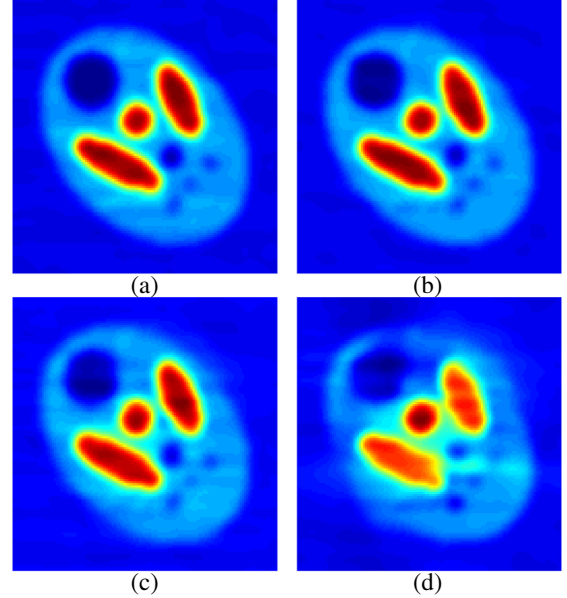


Figure 6. Reconstructions of imaginary part of image with 30 views for different angular coverages: (a) 180°, (b) 150°, (c) 120°, and (d) 90°.

starts showing considerable distortion. This is however not surprising as the restriction of the available data has been limited on both fronts of projections as well as coverage. The process yields better reconstructions from same number of projections when the angular access is higher or more complete. The interesting observation here is that as the coverage decreases from 180° to 120°, the degradation in the image quality is marginal and maybe considered acceptable based on the application. Detailed error analysis has been done in the next section of this chapter. From Fig. 5 to Fig. 10, the reconstructions of real and imaginary parts have been shown separately for angular sweeps as the number of projections is progressively decreased. With higher angular coverage, the reconstruction quality is maintained at up to 20 projections. Significant degradation is observed at 15 projections. This illustrates that as long as the coverage is high, the random sampling and l_1 minimization can perform good reconstructions from very few projections. As the coverage is lowered, acceptable reconstruction is maintained at up to 120°. For even lower coverage, the l_1 minimization alone is not effective. This is because the minimum data requirement even under sparse reconstruction is being violated. In the following section quantitative error analysis has been done on these reconstructions.

4.2. Error Analysis

In order to quantitatively evaluate the reconstructions performed, the Mean Absolute Error (MAE) described in [4] is used again. It is the average of the pixel-by-pixel sum of the absolute difference between the reference and reconstructed image and is given by: $MAE = \frac{1}{n} \sum |img_{orig}(i) - img_{recon}(i)|$, where $img_{orig}(i)$ is the i th pixel in the original image and $img_{recon}(i)$, the i th pixel in the reconstructed image and n is the total number of pixels in the image. The error for the real and imaginary part are calculated separately. For this analysis, additional reconstructions for a coverage range of 60° is also considered. The relative percentage change in MAE for different projection numbers and angular access are shown in Figs. 11–14.

Figures 11 and 12 show the MAE increase for a fixed angular coverage as the number of projections change. The MAE from the maximum number of projections (60) is taken as the base reference to which the percentage change of error is measured as the number of projections is progressively lowered

up to 15. This change is plotted for different angular coverages between 60° to 180° . Fig. 11 shows the performance for the real part of the reconstructed image and Fig. 12 for the imaginary part. As expected, for each angular coverage, as the available number of projections is reduced, the error increases, as seen from the plots.

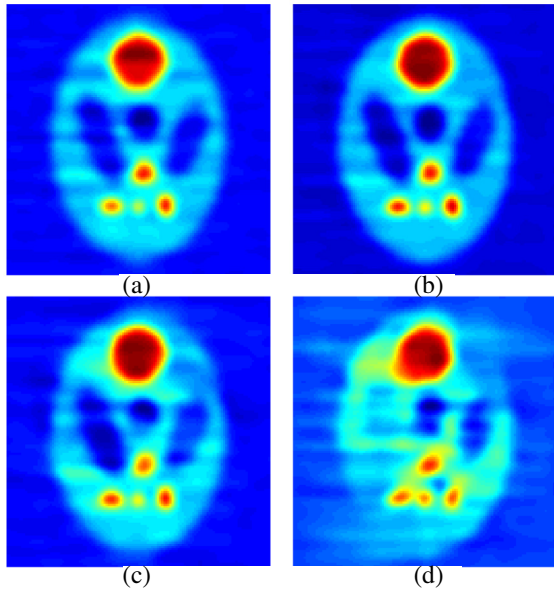


Figure 7. Reconstructions of real part of image with 20 views for different angular coverages: (a) 180° , (b) 150° , (c) 120° , and (d) 90° .

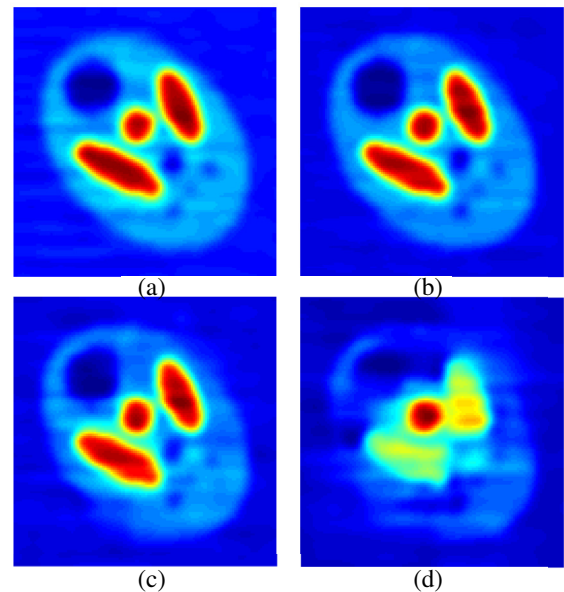


Figure 8. Reconstructions of imaginary part of image with 20 views for different angular coverages: (a) 180° , (b) 150° , (c) 120° , and (d) 90° .

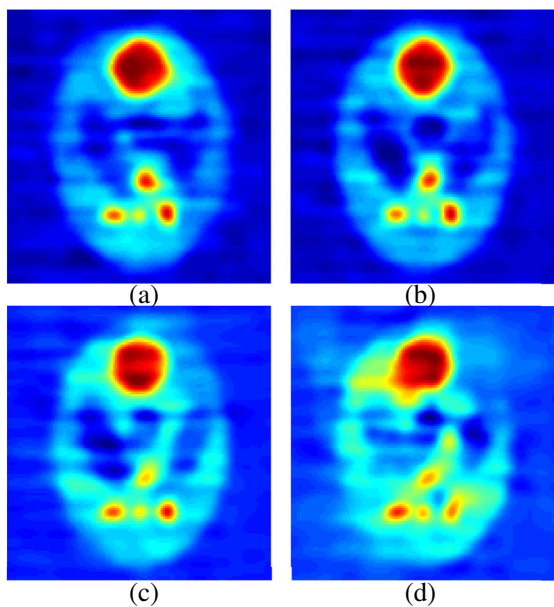


Figure 9. Reconstructions of real part of image with 15 views for different angular coverages: (a) 180° , (b) 150° , (c) 120° , and (d) 90° .

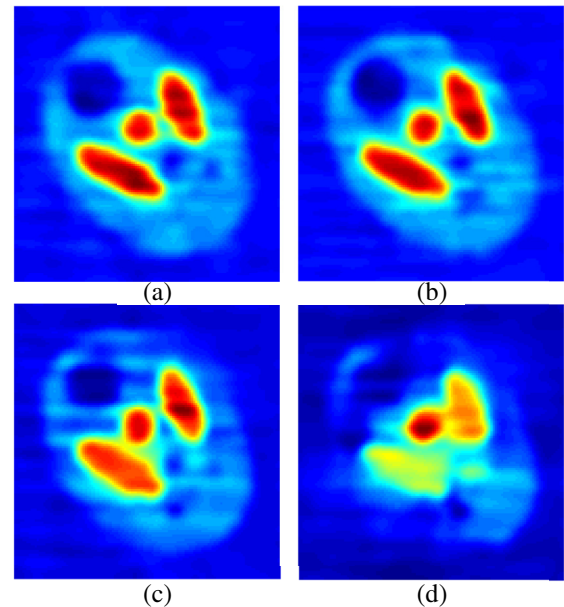


Figure 10. Reconstructions of imaginary part of image with 15 views for different angular coverages: (a) 180° , (b) 150° , (c) 120° , and (d) 90° .

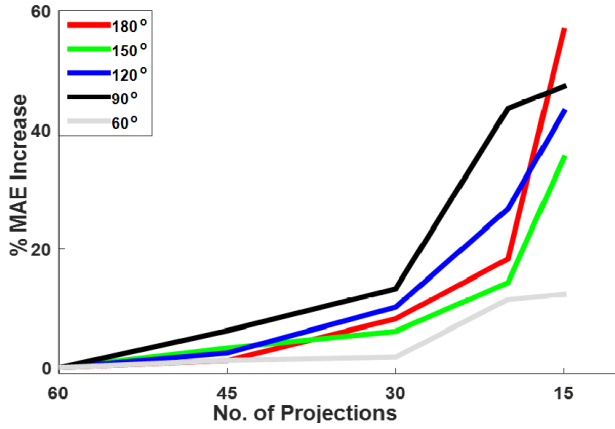


Figure 11. Percentage increase of MAE for real part of image as the number of projections is lowered for a fixed coverage. Graphs plotted for different coverages.

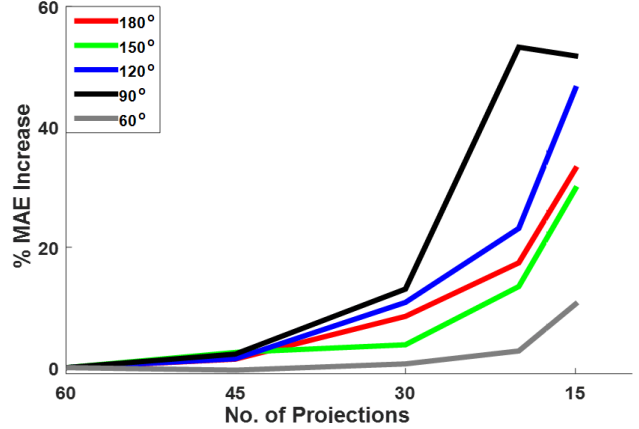


Figure 12. Percentage increase of MAE for imaginary part of image as the number of projections is lowered for a fixed coverage. Graphs plotted for different coverages.

The percentage increase remains below 20% for all coverages at 30 views. From 20 views or less, the error rate increases sharply, e.g., in the real part of the image, the MAE increase for 180° coverage at 20 views is 18% and 56.7% for 15 views. For 120° coverage, the values are respectively 26.7% and 43%. With respect to visual identification of features or defects from reconstructed image, this translates to good reconstructions maintaining all features up to 30 views and acceptable reconstruction at 20 views. At 15 views, the degradation gets considerably high to depend on the images for diagnosis or fault detection with high confidence. An important thing to note here is that in Fig. 11 and Fig. 12, each line shows the percentage increase of error as the view number is decreased while the coverage is fixed. So, although all the plots start at 0% error increase, the actual error value would be higher for a lower coverage, and vice versa. The total coverage determines the extent of data availability for reconstruction. Hence, the change in percentage MAE increase is more striking for higher angular coverages than lower ones. This is illustrated through the plots themselves. The percentage change for 60° is 10.5% in real and 12.4% in imaginary part at 15 projections which is the lowest change observed. This is because the starting point itself is already much worse due to limited coverage and in effect does not get worse with lower number of projections. The observed percentage change in error increases with increasing angular coverage. The MAE plots show that with higher access, the reconstruction accuracy increases.

Another avenue to explore is to observe the effect of the available angular access for a fixed number of projections. This effect is illustrated in Fig. 13 and Fig. 14. Here, for a fixed number of projections, the percentage MAE error is calculated with respect to the maximum angular coverage (180°). The coverage is decreased to 60°. The process is repeated while varying the number of projections from 60 to 15. A similar trend is observed as in the last case. For each fixed projection number, the MAE error increases as the total coverage decreases. This is expected. However, a surprising and appealing fact is that the increase in error is marginal irrespective of total number of projections between 180° to 120°. This illustrates the stability and utility of this CS based reconstruction procedure. The procedure would be handy in either lower angular access or a sparse projection dataset (and up to a certain limit when both constraints are simultaneously present). This puts this CS based framework in a strong position to handle highly adverse data acquisition conditions.

In summary from these reconstruction sets it can be concluded that at 120° coverage, as little as 20 projections might be sufficient for a reasonably accurate reconstruction. This is definitely a great improvement over other traditional iterative methods. For comparison between CS based reconstruction and traditional LS reconstruction, see Fig. 2 from Subsection 2.2.

Further restrictions would be too limiting for reconstruction in a generalized setup of complex valued image with no prior information or known restrictions. However when we have some a-priori

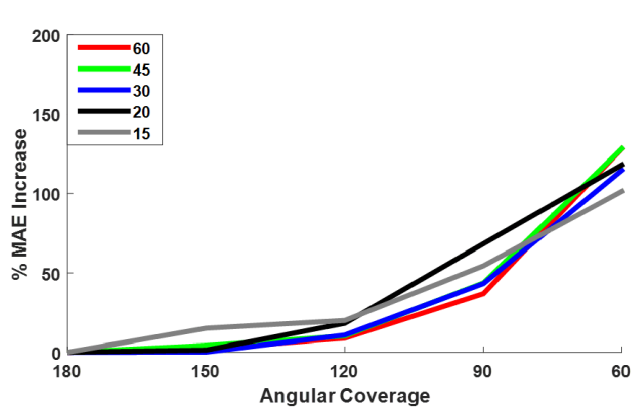


Figure 13. Percentage increase of MAE for real part of image as the angular coverage is lowered for a fixed number of projections. Graphs plotted for different number of projections.

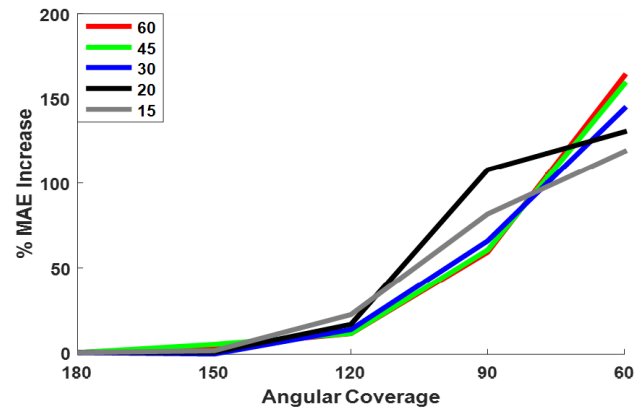


Figure 14. Percentage increase of MAE for imaginary part of image as the angular coverage is lowered for a fixed number of projections. Graphs plotted for different number of projections.

knowledge, either about the structure or some practical insights about the imaged system or ROI, tighter bounds might be achievable as will be demonstrated briefly in the next subsection.

4.3. Reconstruction from Phantoms with Realistic Permittivity Distribution

In practical scenarios, e.g., in microwave tomography, the physical distribution of permittivity variation in the real and imaginary parts would be same, i.e., the real and imaginary parts of the complex valued image would have the same spatial variations and would essentially be visually identical. In this section some reconstructions from a more realistic phantom is shown. The imaginary part of the phantom is kept the same as the real with respect to the shape, as expected in practical measurements. However, the magnitude has been scaled by half. This is reasonable, as in complex permittivity, the imaginary part is much lower than the real part. Because of this simplification, the data requirement would be looser than in the last section and expected to produce better reconstructions under comparable data constraints. Reconstructions from 15 and 10 projections from different angular coverage are given in Fig. 15–Fig. 18. As is evident, for 15 views, there is almost distortionless reconstruction up to 120° and acceptable even at 90° coverage. The imaginary part shows more degradation than the real part at lower coverage. This is because the magnitude of the imaginary components being half of that in the real part and as such, is more susceptible to degradation in general and especially under sparse data recovery conditions. For 10 views, the real part is well retained up to 120° , however, below 150° , the imaginary part degrades considerably. In conclusion, we see that for 15 projections, acceptable reconstruction can be achieved at 120° and for 10 views at 150° . At full 180° , even 10 views can generate a clear reconstruction, maintaining all features distinctly.

For any measurement system, noise is an integral part. The robustness of any reconstruction algorithm is dependent on the noise margins it can handle. So far, the reconstructions have been done with 5% noise. However, to see the effect of increasing noise in the data, reconstructions were performed under various levels of noisy data. The effect was observed on reconstruction from 15 views and 120° angular coverage. The effect of noise is seen in Fig. 19, Fig. 20. The reconstruction is good at 10% noise. The real part is still acceptable at 20% noise, however, the imaginary part is considerably degraded. At 50% noise both real and imaginary parts are highly degraded and unacceptable for visual analysis. However, it should be noted that this is too high a noise margin, which should require improvements in the physical acquisition system rather than the reconstruction algorithm itself. In conclusion, it can be inferred that with TV based CS reconstruction, acceptable reconstruction of complex valued objective function can be achieved from moderately noisy data with as limited coverage as 120° and as little measurements as 15 projections. This is a significant contribution and of value in numerous scenarios with either highly limited angular access or various constraints (like available acquisition time) limiting

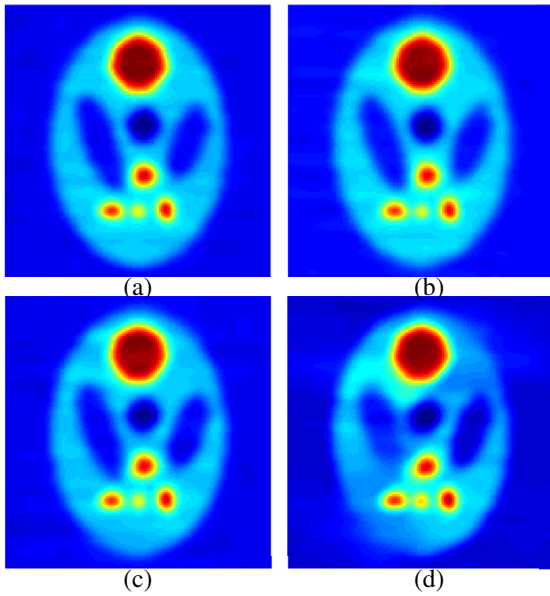


Figure 15. Recovery with symmetric phantoms (visually identical real and imaginary parts): Reconstructions of real part of image with 15 views, for different angular coverages (a) 180°, (b) 150°, (c) 120°, and (d) 90°.

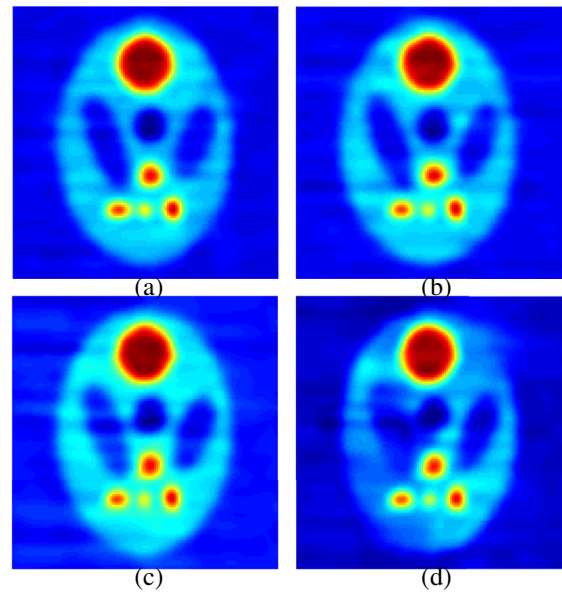


Figure 16. Recovery with symmetric phantoms (visually identical real and imaginary parts): Reconstructions of imaginary part of image with 15 views, for different angular coverages (a) 180°, (b) 150°, (c) 120°, and (d) 90°.

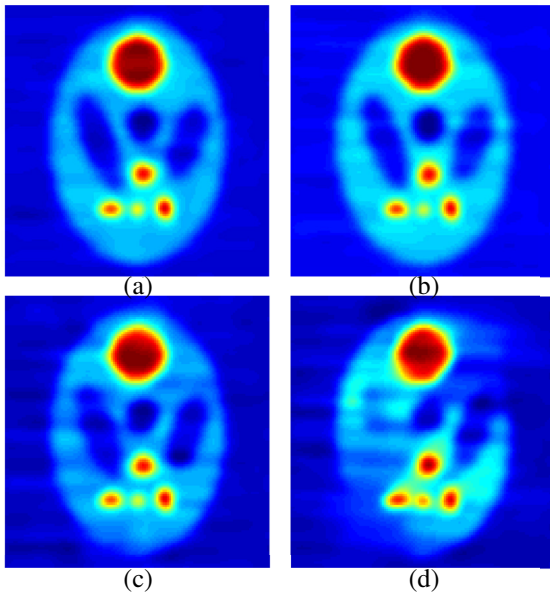


Figure 17. Recovery with symmetric phantoms (visually identical real and imaginary parts): Reconstructions of real part of image with 10 views for different angular coverages (a) 180°, (b) 150°, (c) 120°, and (d) 90°.

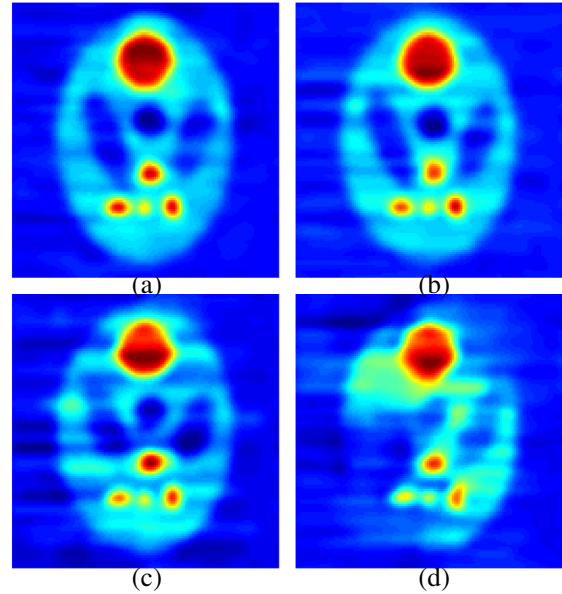


Figure 18. Recovery with symmetric phantoms (visually identical real and imaginary parts): Reconstructions of real part of image with 10 views for different angular coverages (a) 180°, (b) 150°, (c) 120°, and (d) 90°.

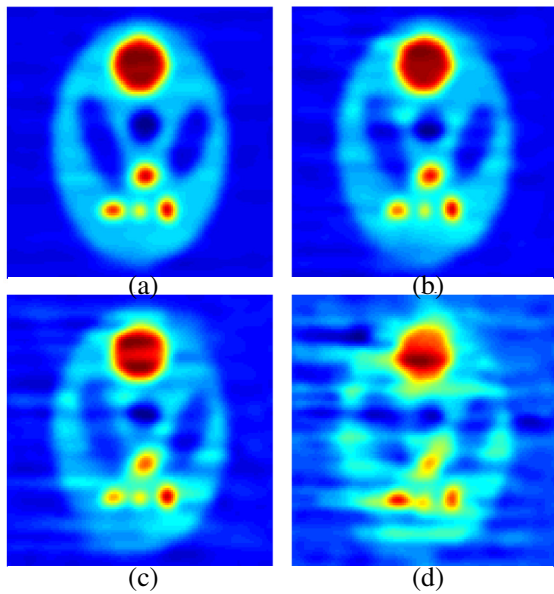


Figure 19. Effect of noise: Reconstructions of real part of image with 15 views and 120° coverage, when real and imaginary parts have similar physical boundaries, for different noise levels (measured as % of mean signal energy level) (a) 5%, (b) 10%, (c) 20%, and (d) 50%.

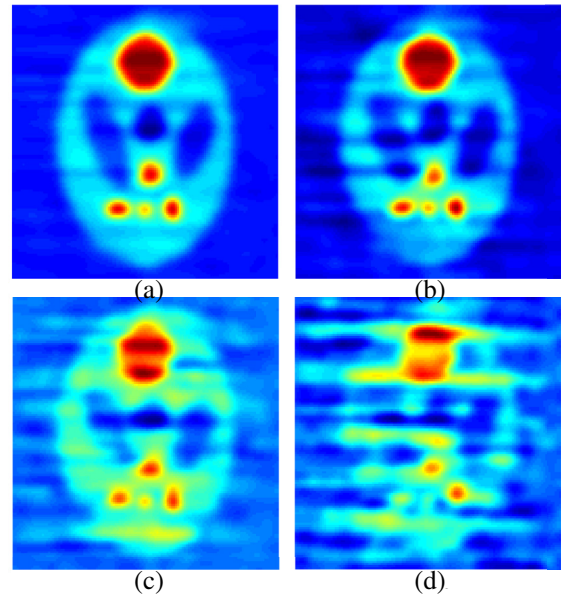


Figure 20. Effect of noise: Reconstructions of imaginary part of image with 15 views and 120° coverage, when real and imaginary parts have similar physical boundaries, for different noise levels (measured as % of mean signal energy level) (a) 5%, (b) 10%, (c) 20%, and (d) 50%.

the total number of projections that can be obtained. With an aim to explore other avenues which might also have pertinent effect towards lowering data requirements in tomographic reconstruction, effect of incorporating multiple sparsity promoting factors is briefly explored in the next section.

5. MULTIPLE SPARSE DOMAIN INCORPORATION

The fundamental principle underlying compressed sensing based signal recovery is to exploit a sparse representation of the signal. If a signal could be represented in multiple sparse domains, it would be interesting to see if these domains could be used simultaneously for better reconstruction. Traditionally wavelets have provided a popular sparse domain in image processing and has been used in CS based reconstructions with great success. It would be instructive to see if wavelets could be incorporated as an added sparse domain in recovery of complex valued objects as well. If a basic wavelet based penalty term can be incorporated to get an acceptable level of reconstruction, a vast bank of wavelet/curvelet/coiflet based filters open up and provide opportunity for further research towards utilizing multiple sparse representations for increasing reconstruction efficiency or lowering data requirements further. Here a basic wavelet penalty term has been incorporated using Haar wavelets. The main aim is to explore the possibility of incorporating multiple sparse domains easily for complex-valued image reconstruction from sparse data. To incorporate the wavelet sparsity term, the optimization problem of (12) is modified as

$$\min_s \{ G(s) = \|F - \Phi \Psi s\|_2^2 + \alpha TV(\Psi s) + \beta \|s\|_1 \} \quad (13)$$

In the above equation, Ψ is the Haar wavelet operator so that $\Psi * f_d$ is the wavelet domain representation of the image f_d . β is the regularization parameter for the second l_1 penalty term. In the following reconstructions, $\alpha = 0.2$ and $\beta = 0.1$ has been used. In Fig. 21, Fig. 22, reconstruction has been performed by solving the optimization problem in Eq. (13) for 15 projections at different angular coverages.

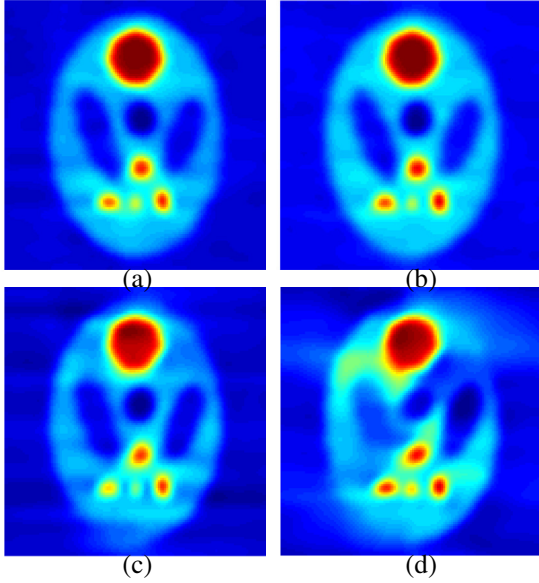


Figure 21. Exploiting multiple sparse domains: Reconstructions of real part of image from 5% noisy data with 15 views, when real and imaginary parts have similar physical boundaries, for different angular coverages: (a) 180°, (b) 150°, (c) 120°, and (d) 90°.

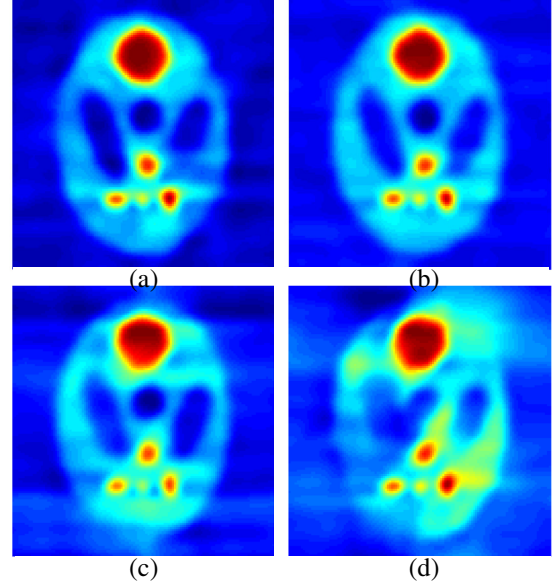


Figure 22. Exploiting multiple sparse domains: Reconstructions of imaginary part of image from 5% noisy data with 15 views, when real and imaginary parts have similar physical boundaries, for different angular coverages: (a) 180°, (b) 150°, (c) 120°, and (d) 90°.

It is interesting to note that the reconstructions are comparable for 180° and 150° coverage but degrades more rapidly than the TV based reconstruction at lower coverage and especially for the imaginary part. There are two possible reasons behind this. Firstly, for these reconstructions, Haar wavelets have been used for wavelet domain representation. This is the simplest wavelet available. Further sophisticated wavelets would actually be much more effective in better sparse representation. Secondly, once a more optimal wavelet is determined, the regularization factors can be optimized to set up a more efficient optimization problem which will generate better reconstructions by truly exploiting the sparsity in multiple domains in parallel. From this experiment, it is apparent that multiple sparsity promoting terms can be simultaneously incorporated in a CS based recovery. Further, there is a huge potential of improvement by using more optimal wavelets than the Haar wavelet used here.

6. CONCLUSION

This paper presents image reconstruction techniques using TV as the sparse l_1 -norm under the compressed sensing regime. Complex valued image reconstruction has been performed with simulated projection data. Hence, this work extends the applicability of CS based DT image recovery for complex valued objective functions. Application areas are many, e.g., recovery of complex permittivity in microwave tomography or complex refractive index in optical diffraction tomography, quantum state tomography etc.. TV based CS algorithms were shown to recover complex valued images from as few as 15 measurements and 120° coverage without any major artifact and retaining all image features distinctly. The noise analysis shows that the algorithms can perform robustly with noisy data. Thus the data requirement for good quality reconstructions under this framework is very low and supports image recovery in all scenarios where highly limited projection data is available due to challenges of limited angular access or small time-frames for data acquisition. The use of multiple sparse domains was also explored. Sample reconstructions were performed using both gradient magnitude of image and Haar wavelets as sparse domains. The responses could be further improved by exploring more optimum wavelets for this application. This is an area for exploration and an interesting future work for extension of this research.

REFERENCES

1. Kak, A. C. and M. Slaney, "Principles of computerized tomographic imaging," *Society for Industrial and Applied Mathematics*, 2001.
2. Paladhi, P., A. Sinha, A. Tayebi, L. Udpa, and A. Tamburrino, "Data redundancy in diffraction tomography," *2015 31st International Review of Progress in Applied Computational Electromagnetics (ACES)*, 1–2, March 2015.
3. Paladhi, P. R., A. Tayebi, L. Udpa, S. Udpa, and A. Sinha, "Class of backpropagation techniques for limited-angle reconstruction in microwave tomography," *AIP Conference Proceedings*, Vol. 1650, No. 1, 509–518, 2015.
4. Paladhi, P. R., A. Sinha, A. Tayebi, L. Udpa, and S. S. Udpa, "Improved backpropagation algorithms by exploiting data redundancy in limited-angle diffraction tomography," *Progress In Electromagnetics Research B*, Vol. 66, 1–13, 2016.
5. Paladhi, P. R., J. Klaser, A. Tayebi, L. Udpa, and S. Udpa, "Reconstruction algorithm for limited-angle diffraction tomography for microwave NDE," *AIP Conference Proceedings*, Vol. 1581, No. 1, 1544–1551, 2014.
6. LaRoque, S. J., E. Y. Sidky, and X. Pan, "Accurate image reconstruction from few-view and limited-angle data in diffraction tomography," *JOSA A*, Vol. 25, No. 7, 1772–1782, 2008.
7. Sung, Y. and R. R. Dasari, "Deterministic regularization of three-dimensional optical diffraction tomography," *JOSA A*, Vol. 28, No. 8, 1554–1561, 2011.
8. Donoho, D. L., "Compressed sensing," *IEEE Transactions on Information Theory*, Vol. 52, No. 4, 1289–1306, 2006.
9. Candès, E. J. and M. B. Wakin, "An introduction to compressive sampling," *IEEE Signal Processing Magazine*, Vol. 25, No. 2, 21–30, 2008.
10. Candès, E. J., J. K. Romberg, and T. Tao, "Stable signal recovery from incomplete and inaccurate measurements," *Communications on Pure and Applied Mathematics*, Vol. 59, No. 8, 1207–1223, 2006.
11. Candès, E. J., J. Romberg, and T. Tao, "Robust uncertainty principles: Exact signal reconstruction from highly incomplete frequency information," *IEEE Transactions on Information Theory*, Vol. 52, No. 2, 489–509, 2006.
12. Lustig, M., D. Donoho, and J. M. Pauly, "Sparse MRI: The application of compressed sensing for rapid MR imaging," *Magnetic Resonance in Medicine*, Vol. 58, No. 6, 1182–1195, 2007.
13. Lustig, M., D. Donoho, J. Santos, and J. Pauly, "Compressed sensing MRI," *IEEE Signal Processing Magazine*, Vol. 25, No. 2, 72–82, March 2008.
14. Chartrand, R., "Fast algorithms for nonconvex compressive sensing: MRI reconstruction from very few data," *IEEE International Symposium on Biomedical Imaging: From Nano to Macro, 2009, ISBI'09*, 262–265, 2009.
15. Gamper, U., P. Boesiger, and S. Kozerke, "Compressed sensing in dynamic MRI," *Magnetic Resonance in Medicine*, Vol. 59, No. 2, 365–373, 2008.
16. Hua, S., M. Ding, and M. Yuchi, "Sparse-view ultrasound diffraction tomography using compressed sensing with nonuniform fit," *Computational and Mathematical Methods in Medicine*, Vol. 2014, 2014.
17. Zhu, Z., K. Wahid, P. Babyn, D. Cooper, I. Pratt, and Y. Carter, "Improved compressed sensing-based algorithm for sparse-view CT image reconstruction," *Computational and Mathematical Methods in Medicine*, Vol. 2013, 2013.
18. Mishali, M. and Y. C. Eldar, "From theory to practice: Sub-nyquist sampling of sparse wideband analog signals," *IEEE Journal of Selected Topics in Signal Processing*, Vol. 4, No. 2, 375–391, 2010.
19. Liu, J., C. Z. Han, X. H. Yao, and F. Lian, "A novel compressed sensing based method for space time signal processing for airborne radars," *Progress In Electromagnetics Research B*, Vol. 52, 139–163, 2013.

20. Baraniuk, R. and P. Steeghs, "Compressive radar imaging," *2007 IEEE Radar Conference*, 128–133, 2007.
21. Yang, M. and G. Zhang, "Parameter identifiability of monostatic mimo chaotic radar using compressed sensing," *Progress In Electromagnetics Research B*, Vol. 44, 367–382, 2012.
22. El-Khamy, M., M. Farrag, and M. El-Sharkawy, "Wide-band secure compressed spectrum sensing for cognitive radio systems," *Progress In Electromagnetics Research B*, Vol. 53, 47–71, 2013.
23. Zhang, Y., L. Wu, B. Peterson, and Z. Dong, "A two-level iterative reconstruction method for compressed sensing MRI," *Journal of Electromagnetic Waves and Applications*, Vol. 25, Nos. 8–9, 1081–1091, 2011.
24. Zhang, Y., S. Wang, G. Ji, and Z. Dong, "Exponential wavelet iterative shrinkage thresholding algorithm with random shift for compressed sensing magnetic resonance imaging," *IEEJ Transactions on Electrical and Electronic Engineering*, Vol. 10, No. 1, 116–117, 2015.
25. Zhang, Y., B. S. Peterson, G. Ji, and Z. Dong, "Energy preserved sampling for compressed sensing MRI," *Computational and Mathematical Methods in Medicine*, Vol. 2014, 2014.
26. Devaney, A., "A filtered backpropagation algorithm for diffraction tomography," *Ultrasonic Imaging*, Vol. 4, No. 4, 336–350, 1982.
27. Sung, Y., W. Choi, C. Fang-Yen, K. Badizadegan, R. R. Dasari, and M. S. Feld, "Optical diffraction tomography for high resolution live cell imaging," *Optics Express*, Vol. 17, No. 1, 266–277, 2009.
28. Catapano, I., L. Di Donato, L. Crocco, O. M. Bucci, A. F. Morabito, T. Isernia, and R. Massa, "On quantitative microwave tomography of female breast," *Progress In Electromagnetics Research*, Vol. 97, 75–93, 2009.
29. Drogoudis, D. G., G. A. Kyriacou, and J. N. Sahalos, "Microwave tomography employing an adjoint network based sensitivity matrix," *Progress In Electromagnetics Research*, Vol. 94, 213–242, 2009.
30. Baran, A., D. J. Kurrant, A. Zakaria, E. C. Fear, and J. LoVetri, "Breast imaging using microwave tomography with radar-based tissue-regions estimation," *Progress In Electromagnetics Research*, Vol. 149, 161–171, 2014.
31. Tayebi, A., J. Tang, P. R. Paladhi, L. Udpa, and S. Udpa, "Design and development of an electrically-controlled beam steering mirror for microwave tomography," *AIP Conference Proceedings*, Vol. 1650, 501–508, AIP Publishing, 2015.
32. Tayebi, A., J. Tang, P. R. Paladhi, L. Udpa, S. S. Udpa, and E. J. Rothwell, "Dynamic beam shaping using a dual-band electronically tunable reflectarray antenna," *IEEE Transactions on Antennas and Propagation*, Vol. 63, No. 10, 4534–4539, 2015.
33. Tayebi, A., P. Roy Paladhi, L. Udpa, and S. Udpa, "A novel time reversal based microwave imaging system," *Progress In Electromagnetics Research C*, Vol. 62, 139–147, 2016.
34. Candès, E. J. and T. Tao, "Decoding by linear programming," *IEEE Transactions on Information Theory*, Vol. 51, No. 12, 4203–4215, 2005.
35. Candès, E. and J. Romberg, "Sparsity and incoherence in compressive sampling," *Inverse Problems*, Vol. 23, No. 3, 969, 2007.
36. Boyd, S. and L. Vandenberghe, *Convex Optimization*, Cambridge University Press, 2004.
37. Bronstein, M. M., A. M. Bronstein, M. Zibulevsky, and H. Azhari, "Reconstruction in diffraction ultrasound tomography using nonuniform fit," *IEEE Transactions on Medical Imaging*, Vol. 21, No. 11, 1395–1401, 2002.
38. Liberti, L. and N. Maculan, "Global optimization: From theory to implementation," *Springer Science & Business Media*, Vol. 84, 2006.
39. Sturm, J. F., "Using sedumi 1.02, a matlab toolbox for optimization over symmetric cones," *Optimization Methods and Software*, Vol. 11, Nos. 1–4, 625–653, 1999.